A numerical study of tsunami wave impact and run-up on coastal cliffs using a CIP-based model

X. Z. Zhao[1], Y. Chen[1], Z.H. Huang[2], Z.J. Hu[1], Y.Y. Gao[1]

[1] Ocean College, Zhejiang University, Zhoushan Zhejiang 316021, China
[2] Department of Ocean and Resources Engineering, School of Ocean and Earth Science and Technology, University of Hawaii at Manoa, USA

Correspondence to: Y.Y. Gao (yygao@zju.edu.cn)

Abstract. There is a general lack of understanding of tsunami wave interacting with complex geographies, especially the process of inundation. Numerical simulations are performed to understand the effects of several factors on tsunami wave impact and run-up in the presence of submarine gentle slopes and coastal cliffs, using an in-house code, a Constrained Interpolation Profile (CIP)-based model. The model employs a high-order finite difference method, the CIP method as the flow solver; utilizes a VOF-type method, the Tangent of hyperbola for interface capturing/Slope weighting (THINC/SW) scheme, to capture the free surface; and treats the solid boundary by an immersed boundary method. A series of incident waves are arranged to interact with varying coastal geographies. Numerical results are compared with experimental data and good agreement is obtained. The influences of submarine gentle slope, coastal cliff and incident wave height are discussed. It is found that the tsunami amplification factor varying with incident wave is affected by gradient of cliff slope, and there is a critical value about 45°. The run-up on a toe-erosion cliff is smaller than that on a normal cliff. The run-up is also related to the length of submarine gentle slope with a critical about 2.292m in the present model for most cases. The impact pressure on the cliff is extremely large and concentrated, and the backflow effect is nonnegligible. Results of our work are in high precision and helpful in inversing tsunami source and forecasting disaster.

1. Introduction

Tsunami is one of the most disastrous coastal hazards in the world, which can be caused by earthquake, volcanic eruption and submarine landslide. The 2004 tsunami in Southeast Asia is one of the most destructive tsunami events in human history. There were over one hundred thousand victims in 11 countries during the tsunami period (Liu et al., 2005). In the recent Great East Japan Earthquake and Tsunami in 2001, over 24 thousand people were killed or missing and 300 thousand building damages occurred (Mimura et al., 2011). More serious nuclear disaster at the Fukushima Nuclear Power Plants No.1 was caused by the powerful run-up and destructive force of the tsunami wave. All these events and lessons from the previous tsunami wave disasters indicate that the actual tsunami wave run-up and the corresponding destructive forces were underestimated (Dao et al., 2013).

Investigation of tsunami wave transformation in the near shore area is a feasible approach to learn the action mechanism and to inverse the tsunami source. Post-disaster studies were mostly done through field observations and numerical simulations. The sediments in the near shore area are frequently regarded as traces of a tsunami. Monecke et al. (2008) analyzed sand sheet deposited by the 2004 tsunami and extended tsunami history 1,000 years into Aceh past, pointing out the recurrence frequency of a damage-causing tsunamis. However, due to the strong backflow of tsunami, sediment can be brought back to seaward. Hence, there may be an underestimation of the run-up using sediment information to study paleotsunamis. Dawson (1994) pointed out that the upper limit of sediment deposition lay well below the upper limit of wave run-up which was marked by a well-defined zone of stripped vegetation and soil. Goto et al. (2011) found that previous estimates of paleotsunamis have probably underestimated by considering their newly acquired data on the 2011 Japanese tsunami event.

However, limited by the complexity in field observations, numerical simulation is another effective approach to investigate tsunami. The computational domain should include a large area in which tsunami generates, propagates and inundates (Sim and Huang, 2015). Therefore, shallow water equations (SWE) were popularly used due to the high efficiency. However, it is a problem that when there is interaction between wave and complex geography, SWE is unable to capture flow structures in detail and often underestimates the result (Liu et al., 1991). An amendment is needful to improve the result of SWE with the data from physical experiment or field observation.

Since the available time-series data of tsunami waveform and flow field in the near-shore area is scarce, there is a general lack of understanding of tsunami interacting with complex geography. A more accurate method is required to reproduce the process of tsunami evolution in the coastal area. Due to the development of supercomputing technology and precise numerical algorithm, computational fluid dynamics (CFD) with viscous flow theory and fluid-solid coupling mechanics are capable of dealing with the complex flow problems when geographies exist. Finite difference method is widely used in various CFD models as flow solver. Hitherto, the accuracy of finite difference method is still a great challenge. In this paper, we introduce a CFD model based on constrained interpolation profile (CIP) algorithm. The CIP method was first introduced by Takewaki et al. (1985) as a high order method to solve the hyperbolic partial differential equation. Tanaka et al. (2000) proposed a new version of the CIP-CSL4, which overcomes the difficulty of conservative property. Hu et al. (2009) simulated strongly nonlinear wave-body interactions used a CIP-based Cartesian grid method, and the results were in good agreement with experiment data. Kawasaki et al. (2015) developed a tsunami run-up and inundation model based on CIP method, and high accurate water surface profile was observed by using slip condition on the wet-dry boundary. Fu et al. (2017) simulated the flow past an in-line forced oscillating square cylinder by a CIP-based model. CIP method can be not only applied in CFD, but also has good performance in other areas. Sonobe et al. (2016) employed CIP method to simulate sound propagation involving the Doppler-effect.

It is a significant research project to deal with the free surface problem in CFD. Hirt et al. (1981) put forward a mass conservation method named Volume of Fluid (VOF), which is flexible and efficient for treating complicated free boundary configurations. Based on the principle of VOF, several improved methods were developed: PLIC (Youngs, 1982), THINC

(Xiao et al., 2005), WLIC (Yokoi, 2007) and THINC/SW (Xiao et al., 2011). Yokoi et al. (2013) proposed a numerical framework consisting of CLSVOF method, multi-moment methods and density-scaled CSF model. The framework can well capture free surface flows with complex interface geometries. More recently, conventional VOF has been widely used by combining with various additional scheme. Malgarinos et al. (2015) proposed an interface sharpening scheme on the basic of standard VOF method, which effectively restrained interface numerical diffusion. Gupta et al. (2016) used a coupled VOF and pseudo transient method to solve free surface flow problems, and the numerical solution was compared well with analytical or experimental data. Quiyoom et al. (2017) simulated the process of gas-induced liquid mixing in a shallow vessel, found that the mixing time predicted by EL+VOF was in good agreement with the measurements.

When coastal geographies are included, special handling of solid boundary is required. Peskin (1973) proposed an immersed boundary method (IBM) to treat the blood flow patterns of human heart, and was later introduced to simulate the interactions between solid objects and incompressible fluid flows (Ha et al., 2014; Lin et al., 2015).

CFD is more convenient and economical than laboratorial experiment and field observation. The most attractive feature is that it can provide time-series data of waveform and flow field, which are helpful for a better understanding of the inundation mechanism of wave in near-shore areas. Markus et al. (2014) introduced a Virtual Free Surface (VFS) model, which enabled the simulations of fully submerged structures subjected to pure waves and combined wave–current scenarios. Vicinanza et al. (2015) proposed new equations to predict the magnitude of forces exerted by the wave on its front face. The equations were added in 5 random wave CFD model and good agreement was obtained when compared with empirical predictions.Oliveira et al. (2017) utilized PFEM to simulate complex solid-fluid interaction and free surface, so that a piston numerical wave-maker are implemented in a numerical wave flumes. Regular long wave was successfully generated in the numerical wave flumes.

When efficient numerical algorithm is adopted, CFD numerical simulation can be applied to study the tsunami inundation in coastal areas. However, limited by the computational efficiency and numerical dissipation of finite difference method, the quantity and slenderness ratio of computational grids should be moderate. Because of the high proportion of spatial span in horizontal and vertical in most cases, reasonable abnormal model scale in horizontal and vertical is necessary, similar to laboratorial experiment.

The purpose of present work is to understand the characteristics of a tsunami, helping inverse the generation mechanisms and provide reference for the tsunami forecasting and post-disaster treatment. In this study, tsunami wave impact and run-up on coastal cliffs is simulated using an in-house code, named the CIP-Based model. Considerable attention is paid to the influence of different coastal topographies, steep cliffs on the beach and submerged gentle slopes are considered. Coastal cliffs are one of the common coastal landforms, representing approximately 75% of the world's coastline (Rosser et al., 2005), such as the coast of Banda Aceh in Indonesia and the steep slope at San Martin (António et al., 1993). The existence of cliff can not only influence the impact and run-up of a tsunami wave but also the erosion-deposition. Different layers provide variations in resistance to erosion (Stephenson et al., 2011). Particularly, some coastal cliffs consisting of soft rocks are eroded at the toe (Yasuhara et al., 2002), which makes it easier to be destroyed. It is indispensable to understand the

function of coastal cliffs and submerged gentle slopes during the tsunami wave approaches near shore. The submerged gentle slope such as the continental shelf, affects the waveform evolution and wave celerity before tsunami waves reach the shoreline. Tsunami amplification factor (Satake, 1994), relative wave height, run-up on the cliff and impact pressure will be analyzed in this work.

In this paper, Section 2 describes the governing equations and the numerical methods; Section 3 provides the initial condition and numerical wave-maker; Section 4 presents model validation; Dimensionless analysis is then used to examine the effect of front slope length, depth ratio and cliff angles on the run-up, and impact pressure; finally, the discussion and conclusion are made in Section 5 and 6, respectively.

2 Numerical models

2.1 Governing equations

Our model is established in a two-dimension Cartesian coordinate system, based on viscous fluid theory with incompressible hypothesis. The governing equations are continuity equation and Navier-Stokes equations written as follows

$$\nabla \cdot \boldsymbol{u} = 0 \tag{1}$$

$$\frac{\partial \boldsymbol{u}}{\partial t} + (\boldsymbol{u} \cdot \nabla)\boldsymbol{u} = -\frac{1}{\rho}\nabla p + \frac{\mu}{\rho}\nabla^2 \boldsymbol{u} + f \tag{2}$$

where $\boldsymbol{u}$, t, ρ, p, μ and f are the velocity, time, fluid density, hydrodynamic pressure, dynamic viscosity and momentum forcing components, respectively.

Multiphase flow theory is employed to solve the problem of solid-liquid-gas interaction. A volume function ϕ_m is defined to describe the percentage of each phase in a mesh

$$\frac{\partial \phi_m}{\partial t} + \boldsymbol{u} \cdot \nabla \phi_m = 0 \tag{3}$$

where $m = 1, 2, 3$, indicating liquid, gas, solid respectively, and $\phi_1 + \phi_2 + \phi_3 = 1$.

Physical property, such as the density and viscosity in a mesh, can be calculated by:

$$\lambda = \sum_{m=1}^{3} \phi_m \lambda_m \tag{4}$$

2.2 The fractional step approach

A fractional step approach is applied to solve the time integration of the governing equations (1) and (2). The first step is to calculate the advection term, neglecting the diffusion term and pressure term, as Eq. (5) shows.

$$\frac{\partial \boldsymbol{u}}{\partial t} + (\boldsymbol{u} \cdot \nabla)\boldsymbol{u} = 0 \tag{5}$$

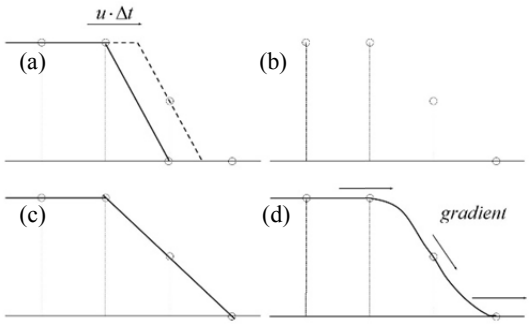

Fig. 1 The principle of CIP method: (a) The solid line is the initial profile and the dashed line is an exact solution after advection, (b) discretized points after advection, (c) linearly interpolated, (d) interpolated using CIP method.

A CIP (Constrained Interpolation Profile) method is employed to solve Eq. (5). The second step is to solve the diffusion term by a central difference scheme

$$\frac{\boldsymbol{u}^{**}-\boldsymbol{u}^{*}}{\Delta t}=\frac{\mu}{\rho}\nabla^{2}\boldsymbol{u}+\vec{F} \tag{6}$$

where $\boldsymbol{u}^{*}$ is the solution of Eq. (5), and $\boldsymbol{u}^{**}$ is the solution to calculate in this step.

The final step is the coupling of the pressure and velocity by considering Eq. (1):

$$\nabla\cdot(\frac{1}{\rho}\nabla p^{n+1})=\frac{1}{\Delta t}\nabla\cdot\boldsymbol{u}^{**} \tag{7}$$

$$\boldsymbol{u}^{n+1}=\boldsymbol{u}^{**}-\frac{\Delta t}{\rho}\nabla p^{n+1} \tag{8}$$

Eq. (7) is solved by a successive over relaxation (SOR) method. More details can be found in our previous works (Zhao et al., 2016a and 2016b).

The free surface is captured by a tangent of hyperbola for interface capturing with slope weighting (THINC/SW) scheme, which is based on the principle of VOF method. The solid boundary is treated by an immersed boundary method (IBM) (Peskin et al., 1973).

2.3 CIP method

The basic principle of CIP is that when computing the advection of a variable *f*, both the transportation equation of *f* and the transportation equation of its spatial gradient $g=\partial f/\partial x$ are used (seen in Fig. 1).

To explain the step of CIP method, we take the following 1D advection equation as an example.

$$\frac{\partial f}{\partial t}+u\frac{\partial f}{\partial x}=0 \tag{9}$$

By differentiating Eq. (9) with respective to *x*, we have the equation about the spatial derivative as

$$\frac{\partial g}{\partial t}+u\frac{\partial g}{\partial x}=-g\frac{\partial u}{\partial x} \tag{10}$$

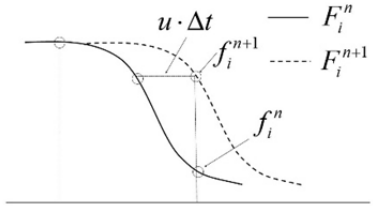

Fig. 2 CIP scheme as a kind of Semi-Lagrangian method

where $g = \partial f / \partial x$. For simplicity, we assume a constant advection velocity. Then Eq. (10) has the same form as Eq. (9). For the case of $u > 0$, we may approximate a profile for f^n inside the upwind cell $[x_{i-1}, x_i]$ as

$$F_i^n(x) = a_i(x - x_i)^3 + b_i(x - x_i)^2 + c_i(x - x_i) + d_i \tag{11}$$

Since, the spatial gradient of f^n can be written as

$$G_i^n(x) = a_i(x - x_i)^2 + b_i(x - x_i) + c_i \tag{12}$$

As shown in Fig. 2 the profile at the time step n+1 is obtained by shifting the profile with $-u\triangle t$, i.e., the time evolution of the function f and g can be obtained by using the following Lagrangian invariants.

$$f_i^{n+1} = F_i^n(x_i - u \cdot \Delta t) \tag{13}$$

$$g_i^{n+1} = G_i^n(x_i - u \cdot \Delta t) \tag{14}$$

Therefore we call the CIP scheme as a Semi-Lagrangian method.

The four unknown coefficients in Eq. (11) can be determined by using known quantities f_i^n, f_{i-1}^n, g_i^n, g_{i-1}^n. It is not difficult to obtain

$$\begin{aligned} a_i &= \frac{g_i^n - g_i^n}{\Delta x^2} - \frac{2\left(f_i^n - f_{i-1}^n\right)}{\Delta x^3}, \quad c_i = g_i^n \\ b_i &= \frac{2g_i^n + g_i^n}{\Delta x} - \frac{3\left(f_i^n - f_{i-1}^n\right)}{\Delta x^2}, \quad d_i = f_i^n \end{aligned} \tag{15}$$

By introducing the spatial gradient of variable f, CIP can provide a third order interpolation function in a single grid. Comparing to traditional upwind schemes, CIP method has not only sub-cell resolution, but also compact high order structure.

2.4 THINC/SW scheme

The THINC/SW scheme, first put forward by Xiao et al. (2011), is used for free surface capturing of incompressible flows. Some test examples has indicated that the scheme has the features we need: mass conservation, a lack of oscillation (Ji et al. 2013). The basic idea of THINC/SW is for the profile of a volume function $\phi\,(0 \le \phi \le 1)$, a hyperbolic tangent function with adjustable parameter is used to interpolate inside an upwind cell, which is shown as follow:

$$\chi_{x,i} = \frac{\alpha}{2}\{1 + \gamma \tanh[\beta(\frac{x - x_{i-1/2}}{\Delta x_i} - \delta)]\} \tag{16}$$

where α, γ, δ, β, are parameters to be specified. α and γ are used to avoid interface smearing, which are given by:

$$\alpha = \begin{cases} \bar{\phi}_{i+1} & \text{if } \bar{\phi}_{i+1} \geq \bar{\phi}_{i-1} \\ \bar{\phi}_{i-1} & \text{otherwise} \end{cases} \tag{17}$$

$$\gamma = \begin{cases} 1 & \text{if } \bar{\phi}_{i+1} \geq \bar{\phi}_{i-1} \\ -1 & \text{otherwise} \end{cases} \tag{18}$$

Parameter δ is used to determine the middle point of the hyperbolic tangent function, and is solved by:

$$\frac{1}{\Delta x_i} \int_{x_{i-1/2}}^{x_{i+1/2}} \chi_i(x) dx = \bar{\phi}_i^n \tag{19}$$

Parameter β determines the steepness of the jump in the interpolation function varying from 0 to 1. In traditional THINC, a constant $\beta = 3.5$ is usually used which may result in ruffling the interface which aligns nearly in the direction of the velocity. To avoid this problem, in THINC/SW, β is determined adaptively according to the orientation of the interface. In a 2D case, β can be written as:

$$\begin{cases} \beta_x = 2.3 \,|\, n_x \,| + 0.01 \\ \beta_y = 2.3 \,|\, n_y \,| + 0.01 \end{cases} \tag{20}$$

3 Simulation setup

3.1 Initial condition

In this section, 2D numerical wave tanks including incident waves and geographies are introduced. Simulation cases are divided into two categories according to different parameters and purposes.

The first simulations are completed in Tank 1, as shown in Fig. 3. This wave tank is 10.0 m in length and 1.0 m in height. Four slopes compose the topography-profile, representing continental slope, continental shelf, beach and cliff, respectively. The still water depth in front of the topography-profile is fixed at 0.35 m, so that the still-water shoreline is located at the starting point of the beach. This point is regarded as the original point of this tank to determine other positions mentioned in this paper. Tank 1 is used for verifying the accuracy of our model and investigating cliff slope gradient and incident wave height, which may influence the tsunami amplification factor. Five cliff slopes are tested: θ_4 = 14°, 21.67°, 39.33°, 49° and 79°. And four incident wave heights are considered: H = 0.025 m, 0.035 m, 0.045 m and 0.055 m. Solitary wave is used as an analogue of tsunami in the numerical modelling. S1~3 in Fig. 3 are three gauges of water elevation, located at x= -7.67 m, -0.87 m and 0.11 m, respectively. Outcomes of S1~3 are used for the comparison between numerical results and experimental data (Sim, 2017). Besides, six gauges of water elevation are employed to calculate the tsunami amplification factor, fixed at x = 0.0 m, 0.06 m, 0.11 m, 0.13 m, 0.16 m and 0.21 m, respectively (not drawn in Fig. 3).

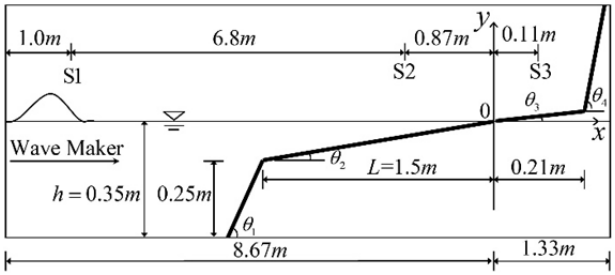

Fig. 3 Schematic diagram of Tank 1. $\tan\theta_1$= 25/17, $\tan\theta_2$= 1/15 and $\tan\theta_3$= 1/30.

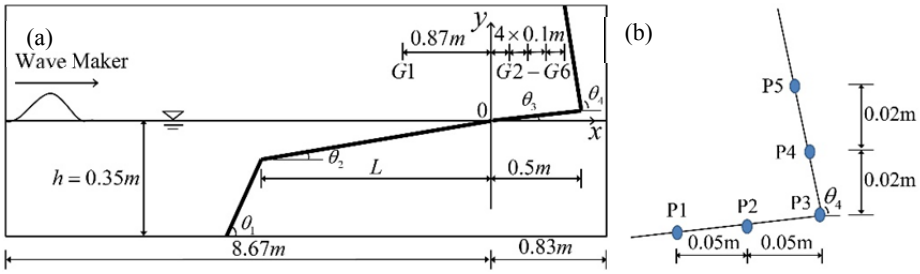

Fig. 4 Schematic diagram of Tank 2. $\tan\theta_1$ = 1.38, $\tan\theta_2$ = 0.08 and $\tan\theta_3$ = 0.02.

The second simulations utilize the Tank 2, similar to the Tank 1 except slight difference, as shown in Fig. 4 (a). In this tank, the still-water shoreline also lies on the starting point of the beach, which is the original point of this tank. Four submarine gentle slopes (standing for continental shelf) of different lengths are used: L = 0.764 m, 1.528 m, 2.292 m and 3.056 m. Three incident wave heights are performed, H=0.04m, 0.05m, 0.06m. Two kinds of cliff, normal cliff of θ_4 = 80.02° degree and toe-eroded cliff of θ_4 = 91.91° degree are considered. Six gauges of water elevation are employed to record the waveform evolution, located at x= -0.87 m, 0.0 m, 0.1 m, 0.2 m, 0.3 m, 0.4 m, respectively. Five pressure sensors are arranged near the toe of the cliff, as shown in Fig. 2 (b). The scales of these two kinds of wave tanks are same to the previous works of (Huang et al., 2013; Sim et al., 2015; Sim, 2017).

In this work, considerable attention will be paid to Tank 2. It is necessary to number the simulated cases in Tank 2 to avoid confusion, as shown in Table 1.

Table 1 Summary of basic parameters calculated in Tank 2

Case	θ_4=80.02° H=0.04 m	θ_4=80.02° H=0.05 m	θ_4=80.02° H=0.06 m	θ_4=91.91° H=0.04 m	θ_4=91.91° H=0.05 m	θ_4=91.91° H=0.06 m
L=0.764 m	1	5	9	13	17	21
L=1.528 m	2	6	10	14	18	22
L=2.292 m	3	7	11	15	19	23
L=3.056 m	4	8	12	16	20	24

3.2 Numerical wave-maker

By declaring a velocity of water particle in the left-most grid and assigning it a value from laboratory wave-paddle velocity, a numerical paddle wave maker is set at the left side of wave tank (Fig. 3 and Fig. 4 (a)).

For a solitary wave, the approximate solution of wave profile near the wave paddle can be described as follow (Boussinesq, 1872):

$$\eta = H \operatorname{sech}^2[\sqrt{\frac{3H}{4h^3}}(ct-\xi)] \tag{21}$$

$$c = \sqrt{g(h+H)} \tag{22}$$

where H, h, c, ξ are the amplitude of the solitary wave, still water depth, wave celerity and wave-paddle trajectory, respectively.

The wave-paddle velocity can be calculated as:

$$u_1(\xi,t) = \frac{d\xi}{dt} \tag{23}$$

For a long wave, the depth-averaged horizontal velocity of water particle derived from continuity equation is expressed as (Mei, 1983):

$$u_2(x,t) = \frac{c\eta(x,t)}{h+\eta(x,t)} \tag{24}$$

The horizontal water particle velocity adjacent to the paddle is equal to the wave-paddle velocity, which means that when $x = \xi$ in Eq. (24), $u_1 = u_2$.

Using Eqs. (24), (26) and (27), wave-paddle trajectory can be derived as an implicit expression:

$$\xi(t) = \sqrt{\frac{4H}{3h}}h \tanh[\sqrt{\frac{4H}{3h^3}}(ct-\xi)] \tag{25}$$

The stroke length of wave-paddle can be calculated as:

$$S = \xi(\infty) - \xi(-\infty) = \sqrt{\frac{16H}{3h}}h \tag{26}$$

In theory, period of solitary wave is infinite. In the application, it can be approximately define as follow:

$$\tanh[\sqrt{\frac{4H}{3h^3}}(c\frac{T}{2}-\frac{S}{2})] = 0.999 \tag{27}$$

$$T = \frac{2}{c}\sqrt{\frac{4h^3}{3H}}(3.8+\frac{H}{h}) \tag{28}$$

The water particle velocity imposed in the left-most grid can be given by:

$$\bar{u}(t) = \frac{c\eta(\xi,t)}{h+\eta(\xi,t)} \quad 0 \le t \le T \tag{29}$$

In our model, the left-most grid is not moveable as laboratory wave-paddle be, modification should be provided to Eq. (29). By some numerical tests, it is finally determined as:

$$\bar{u}(t) = \frac{c[2\eta(\xi(t),t) - \eta(\xi(0),t)]}{h + \eta(\xi(0),t)} \quad 0 \le t \le T \tag{30}$$

4 Numerical result

4.1 Model validation

To verify the accuracy of our model, numerical result from one of the cases in Tank 1 is compared with available experimental data (Sim, 2017). The incident wave height and the cliff slope gradient of this case are H =0.055m and θ_4 = 79 °, respectively. A variable grid is used for the computation, in which the grid points are concentrated near the free surface and the topography. Three non-uniform grids are used to perform a grid refinement test. The grid quantity and the minimum grid size are shown in Table 2.

Table 2 Parameter of three sets of grids (Unit: m)

	Horizontal grid quantity	Vertical grid quantity	Horizontal minimum grid	Vertical minimum grid
Coarse-grid	826	220	0.008	0.0022
Middle-grid	970	320	0.005	0.0015
Fine-grid	1228	468	0.003	0.0008

Fig. 5 concerns the predicted time series of water elevations at different locations S1~3 and the physical measurements (Sim, 2017) are also presented for comparison. Fig. 5 (a) illustrates the comparison results at S1. It can be observed that wave has not reached the topography, so that the waveform has not transformed grossly and is similar to the original waveform. Good general agreement is found for all computations. The relative wave height at S1 is 1.0, which reveals the accuracy of the target incident wave. Fig. 5 (b) shows the results at S2 x = -0.87 m. This gauge point is in the area of the submarine gentle slope, and shoaling happens when wave propagates here. It can be seen from Fig. 5 (b) that the wave front face becomes steep and the back face becomes gentle, which means wave asymmetry appears. Results of three grids are in good agreement with experimental data. Fig. 5 (c) is the most significant among these three graphs, for the gauge station of this graph is located in the front of the cliff where the flow field is extremely complex. Wave rushes from the coastline in a shape of water jet. Then, the water jet impacts the cliff, accompanied by large pressure acting on the toe of cliff. Great acceleration is produced by the impact, making the water run up on the cliff. Under the action of gravity, water finally falls back, large quantity of air is entrained in water when backflow interacts with the incident flow. The velocities of water particles fluctuate violently due to the water-cliff interaction and the drastic water-air mixing. Intense spray of water makes it hard to measure the water elevation with a wave gauge. Hence, Sim (2017) employed three HD Pro c910 web cameras to observe

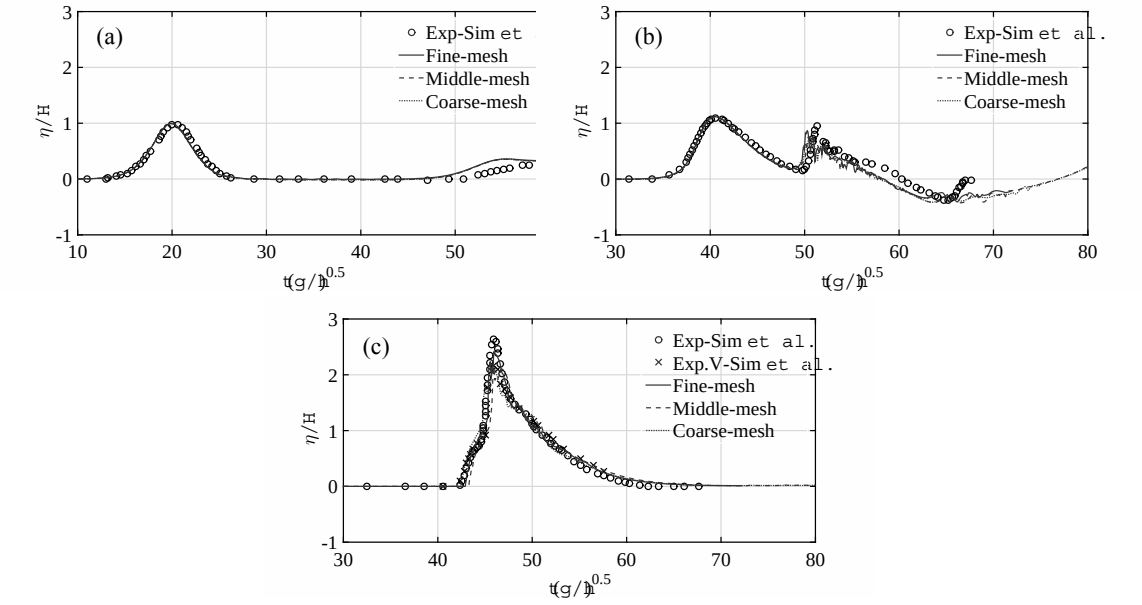

Fig. 5 Time series of experimental data and predicted water elevations using different grids: (a) S1, (b) S2, (c) S3.

wave transformation besides the Ultralab sensors. Data of video recordings from Sim (2017) are also presented in Fig. 5 (c) marked by ×. It can be seen from Fig. 5 (c) that the crest value of video data is 18% smaller than the value of sensor data, which reveals that it is hard to determine the true trace of water surface in such a complex condition. The result of fine-grid is between the result of video data and sensor data, the result of middle-mesh is similar to the video data, and the result of coarse-mesh is 3% smaller than video data. In general, our model shows a good performance in this verifiable example, even when the flow regime is extremely unstable. More verification of our model can been found in Zhao et al. (2014). However, as the coarse-grid has a little underestimation and the fine-grid has low time efficiency, the middle-grid will be adopted to complete the remaining case studies.

4.2 The tsunami amplification factor in Tank 1

Fig. 6 describes the results of the tsunami wave amplification factor in Tank 1. Tsunami amplification factor is defines as a ratio of the local tsunami height to the tsunami height at a reference location. The vertical coordinates are H_m/H_r, in which H_m means the local wave height and H_r means the reference wave height at a reference location x_r. The reference location in present study is x_r= -0.87 m (same as Sim, 2017), and the reference wave height H_r is provided by present numerical result. From the results in Fig. 6, it is observed that there is a critical cliff slope about θ_4=45° . When cliff slope is gentler than the critical value, the tsunami wave amplification factor increases with the increase of the cliff slope gradient. When the slope is steeper than the critical slope, the effect of the cliff slope gradient becomes insignificant. This result is similar to Sim (2017). As for the influence of incident wave height, it can be found in Figs. 6 (e) and (f), of which the wave gauges are close to the cliff. When the cliff slope is gentle, close to θ_4=22°, the tsunami amplification factor increases with the decrease of the

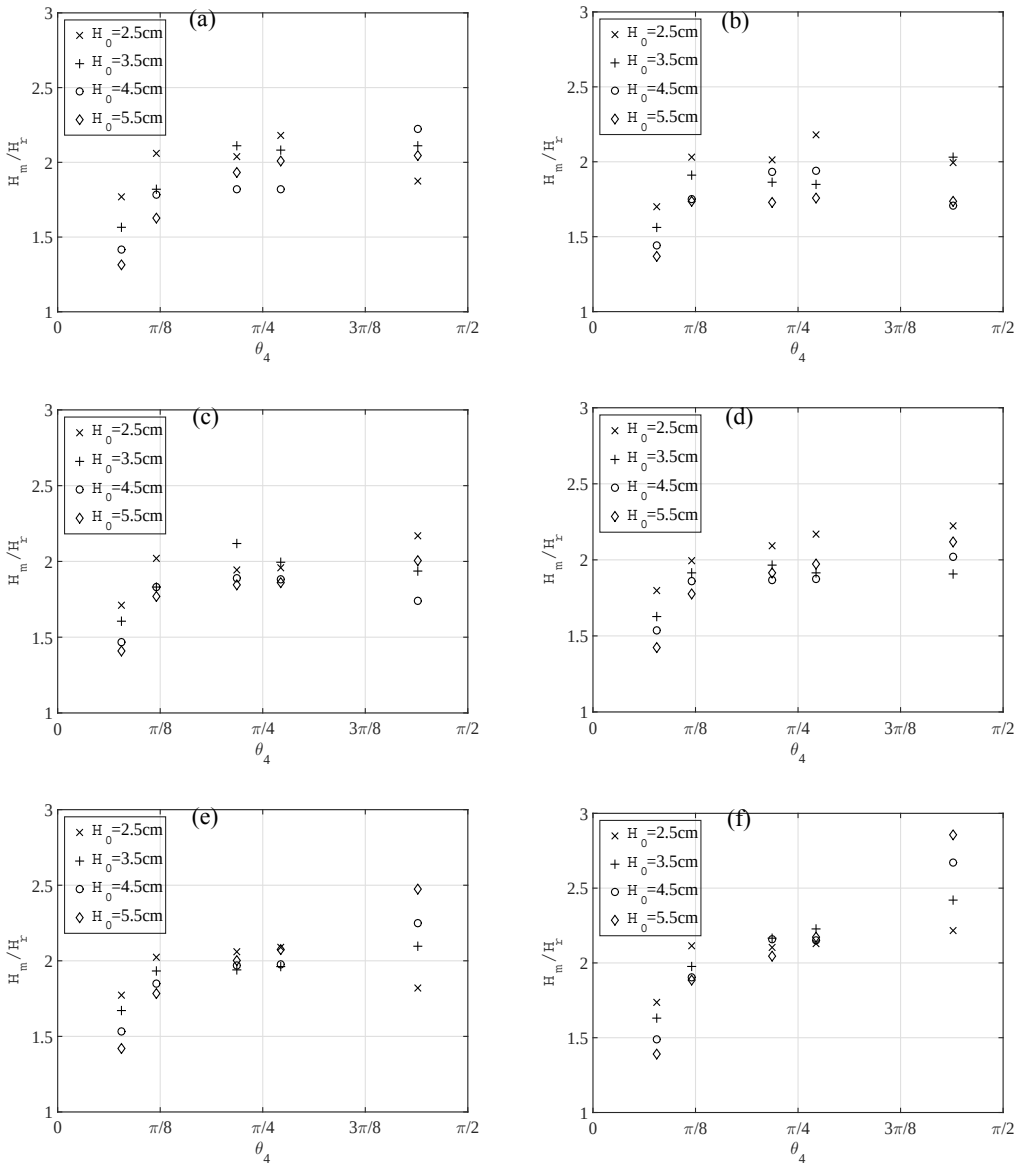

Fig. 6 Wave amplification factors, H_m/H_r of different cliff: (a) x = 0.0 m, (b) x = 0.06 m, (c) x = 0.11 m, (d) x = 0.13 m, (e) x = 0.16 m, (f) x = 0.21 m

incident wave height. As the cliff slope becomes steeper, the effect of different incident waves become negligible at first, and then become important. The critical cliff slope is about θ_4=45°. It is noteworthy that under the condition of steep cliff, the tsunami amplification factor increases with the increase of the incident wave height, in contrast to the gentle cliff. A possible reason for this contrary phenomenon is that the velocity of water particle in the high wave is higher, which allows the high wave easier to run up on the cliff. So that when the cliff slope is gentle, the water of high wave rushes along the cliff and reaches a rearward area, but water of small wave accumulates in the front of cliff. Then, as the cliff slopes get steep, the

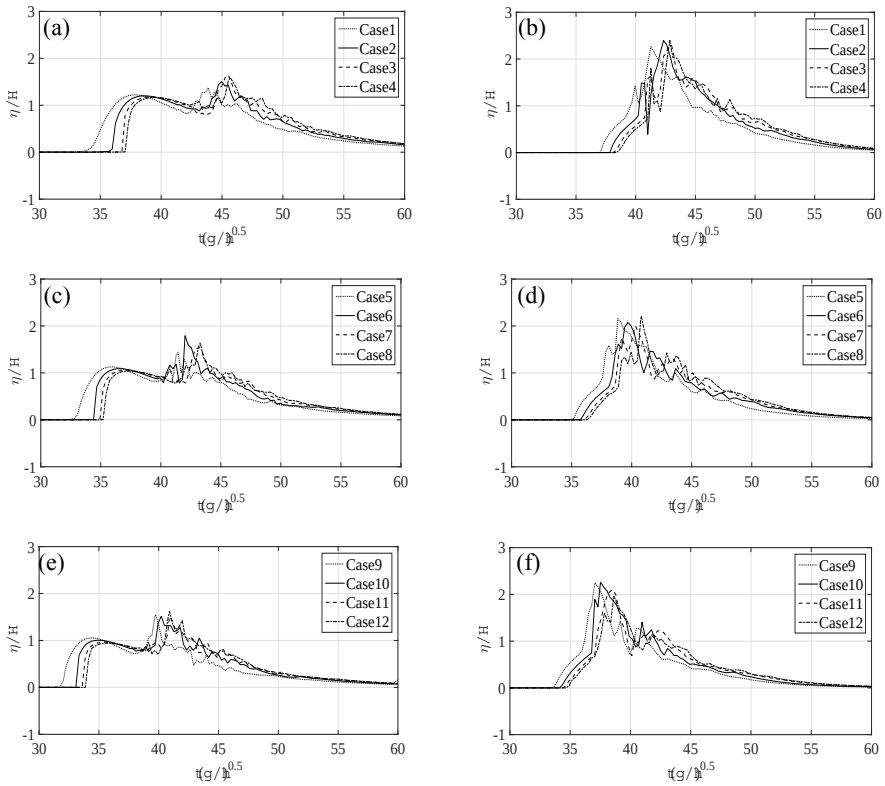

Fig. 7 Time series of relative wave elevation in Tank 2: (a), (c) and (e) x = 0 m; (b), (d) and (f) x = 0.4 m.

so-called rearward area becomes hard to reach for the high wave. This change makes the high wave to accumulate water in the area of these two gauge stations. Moreover, the tsunami amplification factor at these two stations keeps increasing with the increase of the cliff slope angle for a given incident wave, no matter the cliff is steeper or gentler than 45°. Hence, the presence of a cliff does amplify the water elevations on the beach. The influence is particularly evident for the high wave. In present study, the largest tsunami amplification factor is 2.86, as shown in Fig. 6 (f). It is similar with the result of Sim (2017), which has a value of 2.8.

4.3 Time evolution of relative wave elevation in Tank 2

Fig. 7 depicts the time series of relative wave elevation in Tank 2 for the cases 1-12. Four submarine gentle slope lengths and three incident wave heights are considered. The predicted results at x = 0 m are shown in Figs. 7 (a), (c) and (e), whereas at x = 0.4 m shown in Figs. 7 (b), (d) and (f). It can be noticed in Figs. 7 (a), (c) and (e) that there are conspicuous distinctions between the incident and the reflected wave. The relative height of incident wave at x = 0 m increases with the decrease of the initial wave height. The reflected wave fluctuates remarkably because of the complex flow pattern, and the crest reflected wave is higher than the incident wave. As for Figs. 7 (b), (d) and (f), the wave gauges are close to the cliff, it is hard to distinguish the incident and reflected wave. The superposition of incident and reflected wave makes the crest much higher

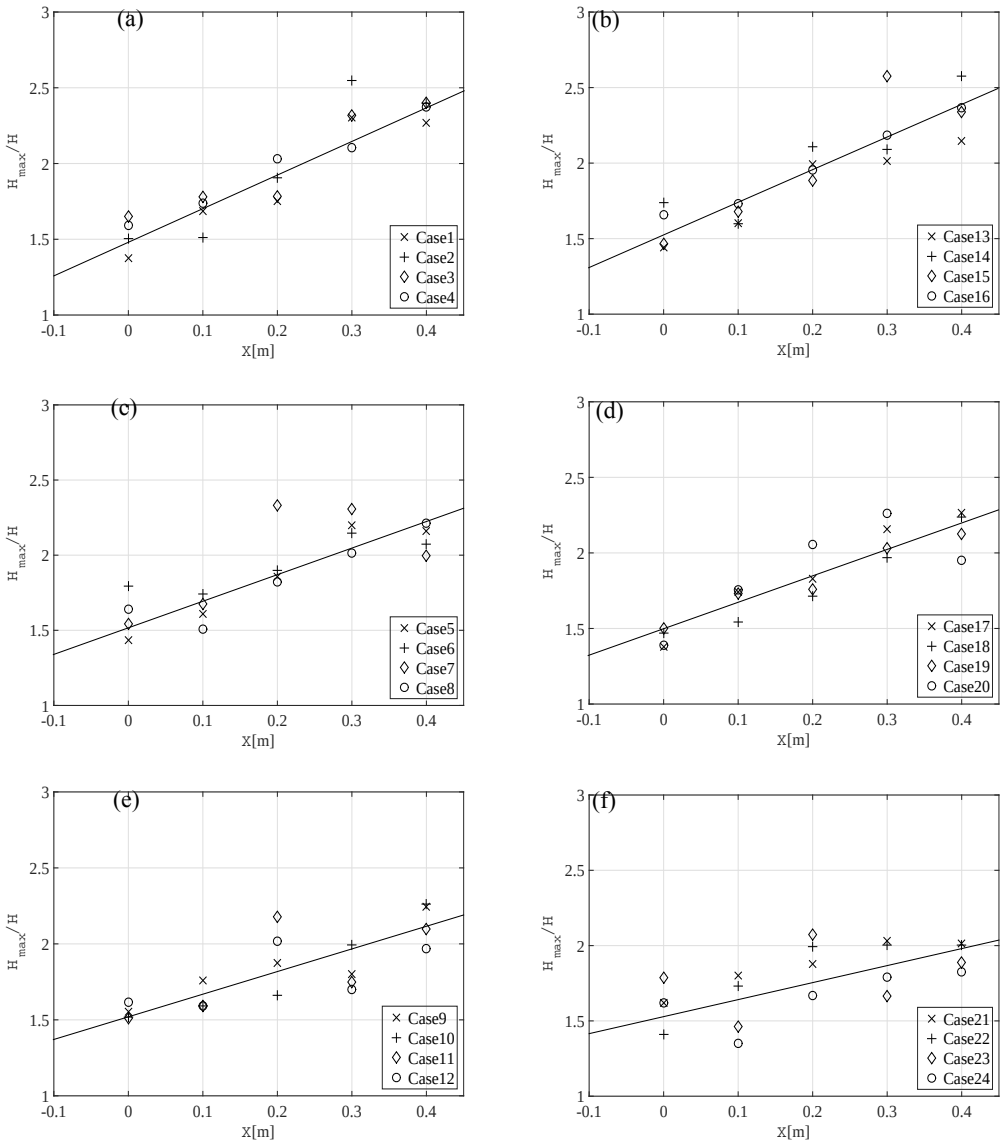

Fig. 8 Maximum relative wave height in front of the cliff in Tank 2: (a) and (b) H = 0.04 m, (c) and (d) H = 0.05 m, (e) and (f) H = 0.06 m.

than the results of Figs. 7 (a), (c) and (e). The effect of initial wave height and length of submarine gentle slope is hard to find from Fig. 7, which remain to the following analysis. The time series results of case13~24 are similar to case1~12, which is not shown here.

4.4 Relative wave height in front of the cliff in Tank 2

Wave heights at five gauges: x=0m, 0.1m, 0.2m, 0.3m and 0.4m, in Tank 2 are shown in Fig. 8. The predicted wave height is normalized to the incident wave height, H. The trend line is also presented as the black lines in Fig. 8. In Figs. 8 (a) and (b),

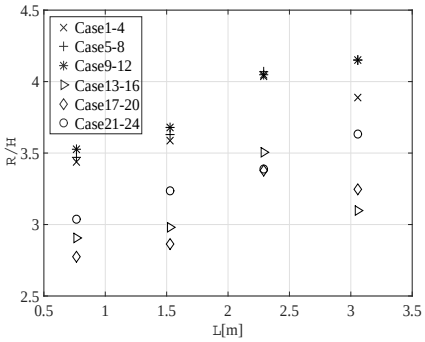

Fig. 9 Wave run-up on the cliff

the maximum relative wave heights are greater than 2.5, and the gradients of trend lines are 2.22 and 2.16, respectively. In Figs. 8 (c) and (d), the maximum relative wave height is 2.4, the trend lines have gradients of 1.77 and 1.75, not as steep as those in Figs. 8 (a) and (b). In Figs. 8 (e) and (f), the trend lines are gentle, with gradients of 1.46 and 1.13. In summary, in the case of smaller wave height, the development of wave height along with the decrease of distance to the cliff is more obvious, and finally a larger relative water height appears. As for lager wave, rate of wave height increase is very small, especially when the cliff is toe-eroded. The possible cause of this interesting phenomenon can be explained as follow. According to the result of Fig. 7, the crest of wave elevation is produced by the mixing of incident and reflected wave. Under the condition of large wave, the reflected wave is very strong, which makes the mixing occupy a wide area on the beach. As a result, energy distribution of large wave is not as concentrated as small wave be. The energy concentration helps the small wave to produce a higher relative wave height near the cliff. It reveals a moderate surface wave magnitude may cause enormous destruction in near-shore areas.

4.5 Wave run-up on the cliff in Tank 2

Fig. 9 displays the wave run-up on the cliff in Tank 2, different lengths of submarine gentle slope are compared. The predicted run-up is normalized to the incident wave height, H. It can be seen in Fig. 9 that there exists a critical length of submarine gentle slope about L=2.292m. When L < 2.292 m, with a given cliff, the relative wave run-up increases as the length of gentle slope increases. When L goes over the critical length 2.292m, the wave run-up fluctuates. When L > 2.292 m, for both normal cliff and toe-eroded cliff, run-up of the case H = 0.04 m decreases, but results of the case H = 0.06 m still increase with the increase of the gentle slope length. Moreover, for cases H = 0.05 m, the normal cliff gives a result of increase and the toe-eroded cliff gives an opposite result. It reveals that the critical value relates to both the incident wave height and the inclination of a cliff. On the other hand, the run-up on normal cliff is higher than on toe-eroded cliff. The maximum relative run-up on normal cliff reaches up to 4.2. The reason is that the inclination of normal cliff is accordant with the direction of the incident wave while the toe-eroded cliff is contrary. Wave can easily climb up on the normal cliff and regurgitate slowly along the cliff. As for the toe-eroded cliff, wave reflects on the cliff and only part of water can run up on the cliff, finally, under the action of gravity, water falls back earlier.

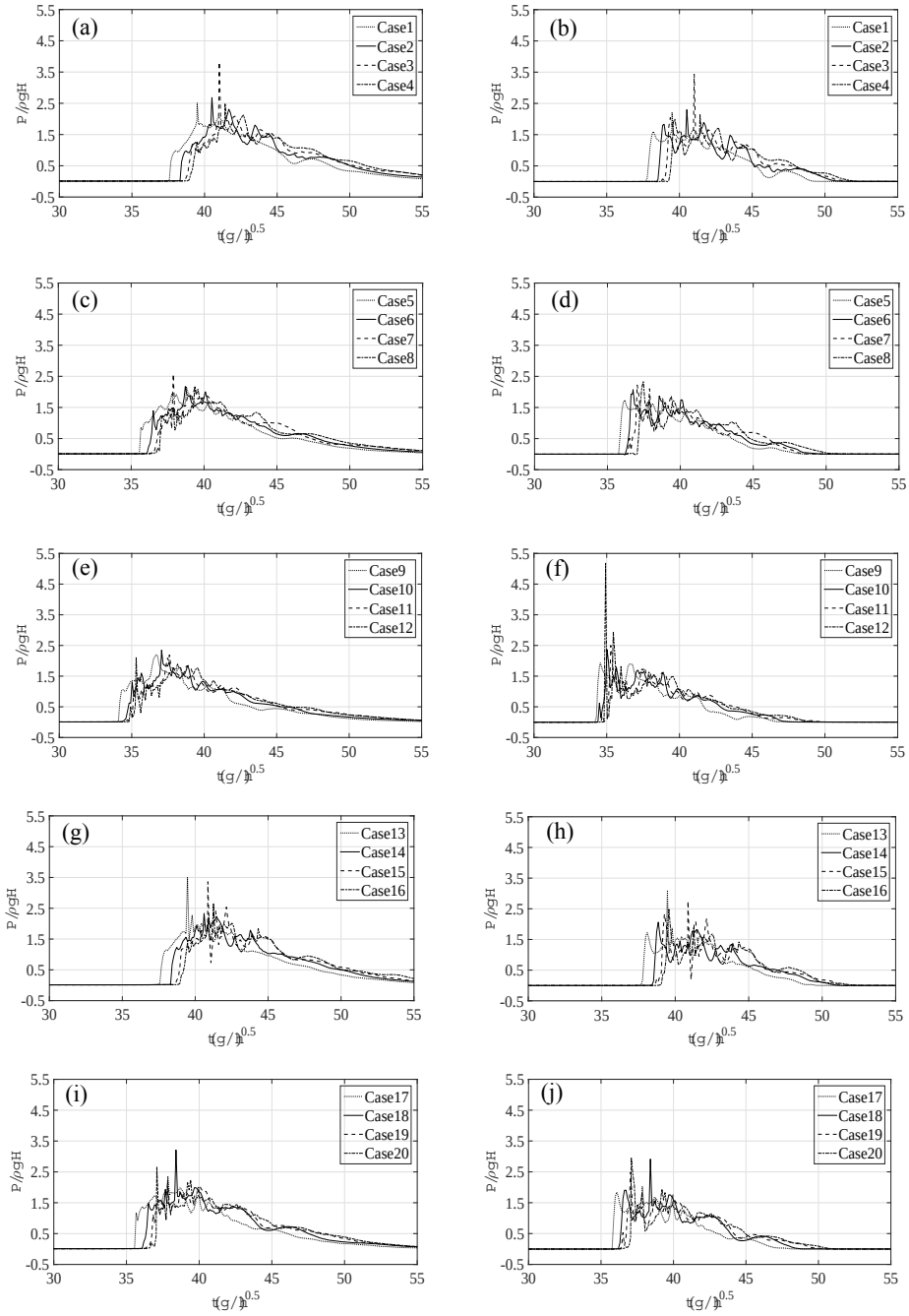
(a)
Case1
Case2
Case3
Case4
(b)
Case1
Case2
Case3
Case4
(c)
Case5
Case6
Case7
Case8
(d)
Case5
Case6
Case7
Case8
(e)
Case9
Case10
Case11
Case12
(f)
Case9
Case10
Case11
Case12
(g)
Case13
Case14
Case15
Case16
(h)
Case13
Case14
Case15
Case16
(i)
Case17
Case18
Case19
Case20
(j)
Case17
Case18
Case19
Case20
P/ρgH
t(g/H)^0.5

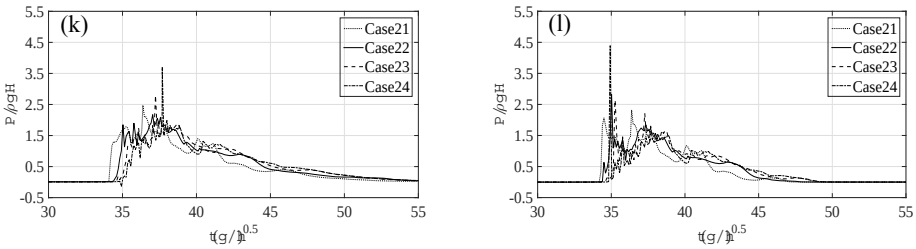

Fig. 10 Time histories of impact pressure on the cliff: (a), (c), (e) , (g), (i), (k) P3; (b), (d), (f), (h), (j), (l) P4.

4.6 Impact pressure analysis in Tank 2

Fig. 10 shows the time histories of impact pressure on the cliff at two pressure sensors P3 and P4. The detailed locations of pressure sensors are shown in Fig. 4 (b). Figs. 10 (a), (c), (e), (g), (i) and (k) give the predicted results at location P3, and the results at location P4 are shown in Figs. 10 (b), (d), (f), (h), (j) and (l). The recorded pressure is normalized to the hydrostatic pressure due to incident wave amplitude, ρgH. The peak pressure can be divided into two categories: the early peak and the later peak, which are caused by the directly impact and backflow, respectively. It is obvious that the high incident wave height is beneficial to the appearance of early peak. Once the early peak appears, it is very larger comparing to the later peak. In the cases of small incident wave height, only later peak is observed at both measurement points. In the action period, besides the pressure peak, the main scope of relative pressure ranges from 1.0 to 2.5.

The maximum pressures at five pressure sensors of all cases are also shown in Fig. 11. According to the analysis of Fig. 10, there is no peak when the maximum relative pressure is smaller than 2.5, here our attention will be paid on maximum relative pressure greater than 2.5. It can be found that the inclination of cliff affects the appearance of the pressure peak. Under the condition of a toe-eroded cliff, the generation of pressure peak is frequent. As for the normal cliff, the pressure peak is rare, but it can be terribly large once it appears. In addition, the pressure peak is found to be related to the length of submarine gentle slope L. When L is small, it is easier for a small wave to generate an extreme pressure, which may be caused by backflow; and when L becomes large, a high wave has a trend to generate an extreme pressure, which is probably caused by the direct wave impact.

Fig. 12 demonstrates the snapshots of the pressure distribution at different time instances. Two typical cases of a normal cliff $\theta_4 = 80.02^\circ$ (case 12) and a toe-eroded cliff $\theta_4 = 91.91^\circ$ (case 24) are shown. The predicted results for the case 12 are shown in Figs.12 (a), (c) and (e), and case 24 are shown in Figs. 12 (b), (d) and (f). Firstly, the wave impacts on the cliff at very onset, extreme pressure distribution appears in a small area at the toe of the cliff, near the location of pressure sensor P4 (Figs. 12 (a) and (b)). Because of the cliff, the wave front is deviated and is deflected to a water jet along the cliff. As the water runs up the cliff and slowed down by the gravity action. Also it seems that the pressure impacting on the cliff has been decreased a little (Figs. 12 (c) and (d)). Moreover, significant water splashing of small water droplets can be observed, contributed from present accurate numerical model. Finally, the water falls back from the cliff due to gravity effect. This

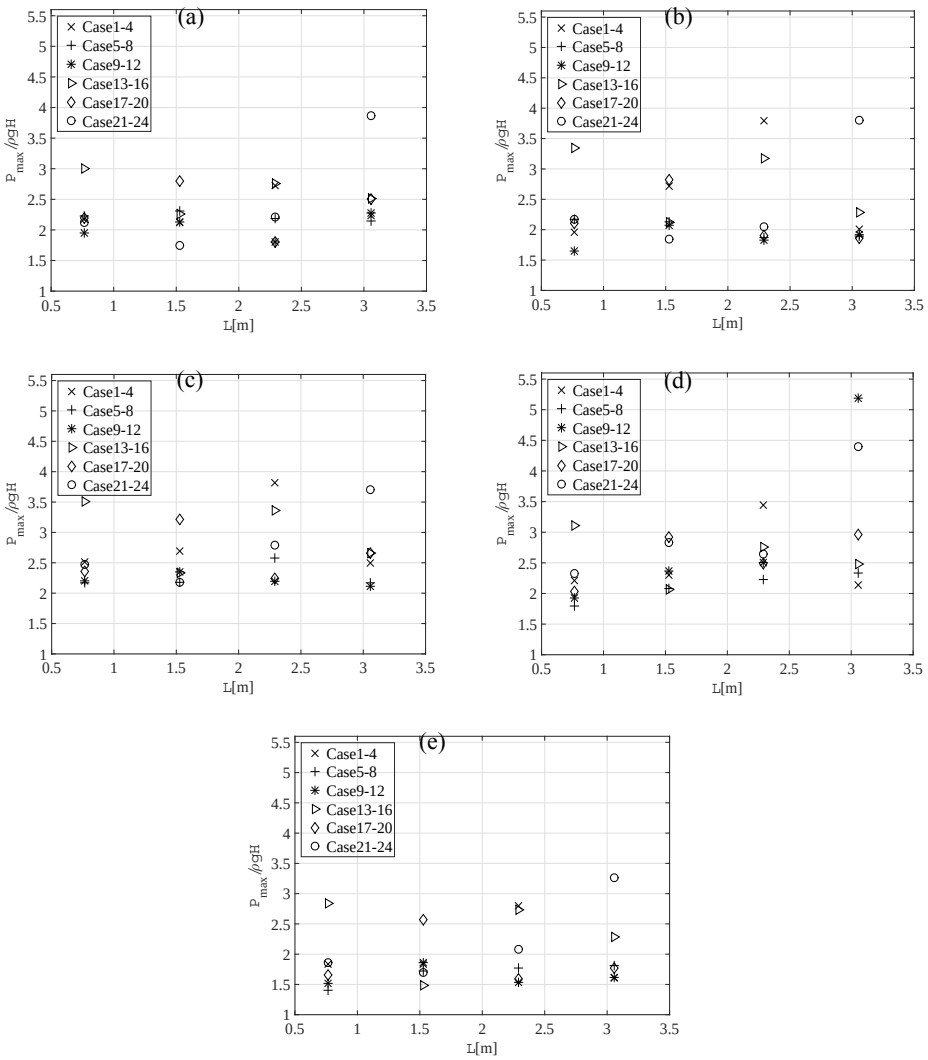

Fig. 11 Maximum impact pressure at five measuing points.

causes the formation of a backward plunging backflow hitting the underlying water, entrapping air. At this stage, extreme pressure appears again and the scope is large, mainly on the beach in front of the cliff. Due to the cliff inclination angle effect, the detailed water flow characteristic on the toe-eroded cliff is found to be different from that on the normal cliff. When the wave propagates along the gentle slope and hits the cliff, the water front horizontal velocity is changed upward along the cliff, as shown in Figs. 12 (a) and (b). As time passes by, the wave run-up on the toe-eroded cliff deviates from the cliff due to gravity effect (Fig. 12 (d)), which will cause a violent plunging breaker onto the underlying water (Fig. 12 (f)). While for a normal cliff, the wave runs up along the cliff, complex backflow is generated and later wave breaking and air-entrainment occurs between the backflow and the underlying water. A comparison of left column and right column of Fig. 12 reveals that although the general key flow features such as water breaking, water splashing and air-entrainment are not

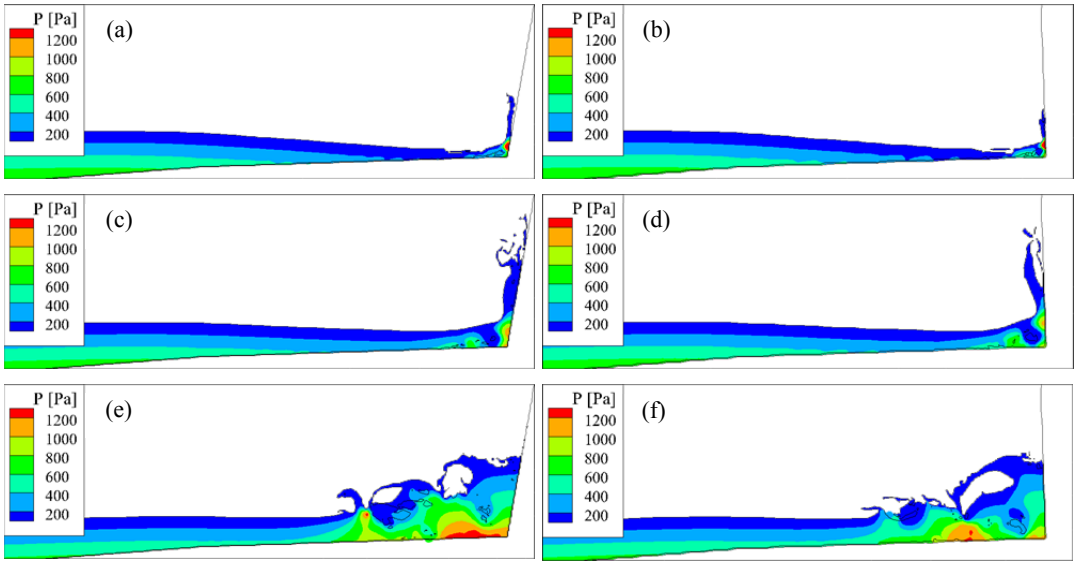

Fig. 12 Snapshots of impact pressure distribution in front of the cliff. (a), (c), (e) case12, (b), (d), (f) case24.

significantly affected by the inclination angle of the cliff, the detailed flow features is different. The above findings are partly consistent with the results of Huang et al. (2013). Combining with the results in Fig. 10, the extreme pressure caused by the direct impact is very large and extraordinarily concentrated, which may destroy the structures and human beings near the coast. While the backflow also produces extreme pressure with a widely affecting area. The worst thing is that it may carry plenty of floats from damaged construction and vegetation, causing secondary damage.

5 Discussion

The tsunami amplification factor is essentially a kind of relative wave height, which normalized to the height at a reference location. The interesting result in present work is as follow. In Tank 1, we analyse the tsunami amplification factor near the steepest cliff and find that it increases with the increase of initial wave height (as Figs. 6 (e) and (f) shown). However, in Tank 2, when the gauge is close to the normal cliff, the relative wave height decrease as the increase of initial wave height (seen in Figs. 8 (a), (c) and (e)). It seems that the results of Tank1 and Tank2 are contradictory. One of the possible explanations is the influence of the beach. The most significant difference between Tank1 and 2 is the length of beach. The effect of beach can be simply summed up as follow. The longer the beach is, the more energy lost before wave impact. The beach is also an area for the mixing of incident and reflected wave, for a large wave which requires a long area to mixing, when the beach is not long enough, the drastic mixing will occur under the coastal line. The Details of beach effect, including process of mixing and energy dissipation, is a meaningful research subject, which remains to the future work.

As for the run-up in Tank 2, a critical length of submarine gentle slope is found for some cases. Before the wave gets across the coastal line, submarine gentle slope facilitates wave deformation and energy focus. A proper slope helps wave to

get an adequate preparation before it touch the cliff. When the slope is too long, as wave getting the shore line, it may have broken be on the verge of breaking, which makes energy dissipate ahead of time. However, the optimum length is effect by several factors such as initial wave height and cliff slope, that's why there is no critical value found in some cases. From the present work, it is reasonable to speculate that higher initial wave require longer submarine gentle slope to achieve the critical value. This can be connected with the analysis of Fig. 11 that when L is small, small wave generates extreme pressure, and when L becomes large, high wave has a trend to generate extreme pressure. On the other hand, normal cliff also enlarge the critical value comparing with toe-eroded cliff. The complicated relationship between these factors needs an even deeper investigation.

The present work is only a start of future work, understanding of tsunami inundation need to be more detailed and quantificational.

6 Conclusions

In this study, tsunami wave impact and run-up in the presence of submarine gentle slopes and a coast cliff are investigated numerically using a CIP-based model. Numerical results are firstly compared with available experimental data and the good agreement revealed the ability of our model to solve the complex flow field, such as wave breaking, water-air mixing and violent impact. The results can be summarized as follows.

(1) The gradient of cliff slope has a critical value about 45°, different characteristics of tsunami amplification factor has been found when the angle is greater or smaller than 45°.

(2) The length of submarine gentle slope influences the tsunami wave run-up, and has a critical value about L = 2.292 m in this study for some cases.

(3) When wave transforms near the cliff, the cases with small incident wave height has a larger relative wave height, which means a devastating tsunami may be caused by a moderate source.

(4) It is easier for tsunami waves to run up on normal cliff than on toe-eroded cliff.

(5) There are two opportunities for the appearance of pressure peak during the process of tsunami wave run-up and impact. One is the direct impacting pressure when tsunami waves first hit the coastal cliff, and the other is caused by the backflow from the cliff after run-up with a widely affecting area.

The present study gives time history of tsunami evolution from open sea to coastal area, which is rare in field study. Several topographies and different incident waves has been considered. Comparing with the SWE result, which may underrate and need amendment, present results can simulate the tsunami in near shore areas more accurately. The present model is helpful for tsunami forecast, dangerous prediction and post-disaster analysis. Furthermore, combining with geology knowledge, the earthquake source magnitude and generation location can be determined.

Acknowlegements

This work was financially supported by the National Natural Science Foundation of China (Grant Nos. 51479175, 51679212), Zhejiang Provincial Natural Science Foundation of China (Grant No. LR16E090002).

References

António M. Baptista, George R. Priest, Tad S. Murty. Field survey of the 1992 Nicaragua tsunami, Marine Geodesy, 1993, 16(16):169-203.

Boussinesq J. Théorie des ondes et des remous qui se propagent le long d'un canal rectangulaire horizontal, en communiquant au liquide contenu dans ce canal des vitesses sensiblement pareilles de la surface au fond [J]. Journal de Mathématiques Pures et Appliquées, 1872: 55-108.

Dao M. H., Xu H., Chan E. S., and Tkalich P. Modelling of tsunami-like wave run-up, breaking and impact on a vertical wall by SPH method, Nat. Hazards Earth Syst. Sci., 2013, 13, 3457-3467.

Dawson A. G. Geomorphological effects of tsunami run-up and backwash, Geomorphology, 1994, 10(1-4):83-94.

Fu Y, Zhao X, Cao F, et al. Numerical simulation of viscous flow past an oscillating square cylinder using a CIP-based model [J]. Journal of Hydrodynamics, Ser. B, 2017, 29(1): 96-108.

Goto K., Chagué-Goff C., Fujino S., et al. New insights of tsunami hazard from the 2011 Tohoku-oki event, Marine Geology, 2011, 290(290):46-50.

Gupta V K, Srikanth K, Punekar H. Improvements in free surface flow numerics using coupled vof and pseudo transient solver[C]//High Performance Computing Workshops (HiPCW), 2016 IEEE 23rd International Conference on. IEEE, 2016: 100-105.

Hu C, Kashiwagi M. Two-dimensional numerical simulation and experiment on strongly nonlinear wave–body interactions [J]. Journal of Marine Science and Technology, 2009, 14(2): 200-213.

Hirt C. W., Nichols B. D. Volume of fluid (VOF) method for the dynamics of free boundaries, Journal of Computational Physics, 1981, 39(1): 201-225.

Ha T, Shim J, Lin P, et al. Three-dimensional numerical simulation of solitary wave run-up using the IB method, 2014, Coastal Engineering, 84:38-55.

Huang Z., Wu T., Chen T., Sim S.Y. A possible mechanism of destruction of coastal trees by tsunamis: A hydrodynamic study on effects of coastal steep hills, Journal of Hydro-environment Research, 2013, 7: 113-123.

Ji Q, Zhao X, Dong S. Numerical study of violent impact flow using a CIP-based model [J]. Journal of Applied Mathematics, 2013, 2013.

Kawasaki K, Suzuki K. Numerical simulation of tsunami run-up and inundation employing horizontal two-dimensional model based on cip method [J]. Procedia Engineering, 2015, 116: 535-543.

Lin P., Cheng L., Liu D. A two-phase flow model for wave-structure interaction using a virtual boundary force method, Computers and Fluids, 2015, 129, 101-110.

Liu Philip L F, Lynett P, Fernando H, et al. Observations by the international tsunami survey team in Sri Lanka, Science, 2005, 308(5728):1595-1595.

Liu Philip L F, Synolakis, et al. Report on the International Workshop on Long-Wave Run-up, Journal of Fluid Mechanics, 1991, 229(-1):675-688.

Mei C C. The applied dynamics of ocean waves [J]. John Wiely & Sons, New York, 1983.

Markus D, Arnold M, Wüchner R, et al. A Virtual Free Surface (VFS) model for efficient wave–current CFD simulation of fully submerged structures [J]. Coastal Engineering, 2014, 89: 85-98.

Malgarinos I, Nikolopoulos N, Gavaises M. Coupling a local adaptive grid refinement technique with an interface sharpening scheme for the simulation of two-phase flow and free-surface flows using VOF methodology [J]. Journal of Computational Physics, 2015, 300: 732-753.

Mimura N., Yasuhara K., Kawagoe S., Yokoki H., and Kazama S. Damage from the Great East Japan Earthquake and Tsunami-A quick report, Mitigation and Adaptation Strategies for Global Change, 2011, 16, 803-818.

Monecke K, Finger W, Klarer D, et al. A 1,000-year sediment record of tsunami recurrence in northern Sumatra, Nature, 2008, 455(455):1232-1234.

Quiyoom A, Ajmani S K, Buwa V V. Role of free surface on gas‐induced liquid mixing in a shallow vessel[J]. AIChE Journal, 2017.

Oliveira T C A, Sanchez-Arcilla A, Gironella X, et al. On the generation of regular long waves in numerical wave flumes based on the particle finite element method[J]. Journal of Hydraulic Research, 2017: 1-19.

Peskin C S. Flow patterns around heart valves, Lecture Notes in Physics, 1973, 10:214-221.Rosser N J, Petley D N. Terrestrial laser scanning for monitoring the process of hard rock coastal cliff erosion, Quarterly Journal of Engineering Geology & Hydrogeology, 2005, 38(11): 363-376.

Stephenson W J, Naylor L A. Within site geological contingency and its effect on rock coast erosion, Journal of Coastal Research, 2011, SI64 (SI64): 831-835.

Sim S Y. Run-up related to onshore tsunami flows, Ph.D Thesis, Nanyang Technological University, Singapore, 2017.

Sim S Y, Huang Z. An experimental study of tsunami amplification by a coastal cliff, Journal of Coastal Research, 2015, 32(3):611-618.

Sonobe T, Okubo K, Tagawa N, et al. A novel numerical simulation of acoustic Doppler effect using CIP-MOC method [J]. The Journal of the Acoustical Society of America, 2016, 140(4): 3249-3249.

Satake K. Mechanism of the 1992 Nicaragua tsunami earthquake [J]. Geophysical Research Letters, 1994, 21(23): 2519-2522.

Takewaki H, Nishiguchi A, Yabe T. Cubic interpolated pseudo-particle method (CIP) for solving hyperbolic-type equations, Journal of Computational Physics, 1985, 61(2):261-268.

Tanaka R, Nakamura T, Yabe T. Constructing exactly conservative scheme in a non-conservative form [J]. Computer physics communications, 2000, 126(3): 232-243.

Vicinanza D, Dentale F, Salerno D, et al. Structural Response of Seawave Slot-cone Generator (SSG) from Random Wave CFD Simulations[C]//The Twenty-fifth International Offshore and Polar Engineering Conference. International Society of Offshore and Polar Engineers, 2015.

Xiao F., Honma Y., Kono T. A simple algebraic interface capturing scheme using hyperbolic tangent function, International Journal for Numerical Methods in Fluids, 2005, 48(9): 1023-1040.

Xiao F., Ii S., Chen C. Revisit to the THINC scheme: a simple algebraic VOF algorithm, Journal of Computational Physics, 2011, 230(19): 7086-7092.

Youngs D. L. Time-dependent multi-material flow with large fluid distortion, Numerical Methods for Fluid Dynamics, 1982, 24, 273-285.

Yokoi K. A practical numerical framework for free surface flows based on CLSVOF method, multi-moment methods and density-scaled CSF model: Numerical simulations of droplet splashing[J]. Journal of Computational Physics, 2013, 232(1): 252-271.

Yokoi, K. Efficient implementation of THINC scheme: a simple and practical smoothed VOF algorithm, Journal of Computational Physics, 2007, 226(2): 1985-2002.

Yasuhara, K., Murakami, S., Kanno, Y., et al. Fe analysis of coastal cliff erosion due to ocean wave assailing, First International Conference on Scour of Foundations. 2002.

Zhao, X., Cheng, D., Zhang, D., et al. Numerical study of low-Reynolds-number flow past two tandem square cylinders with varying incident angles of the downstream one using a CIP-based model, Ocean Engineering, 2016a, 121:414-421.

Zhao, X., Gao, Y., Cao, F. and Wang, X.: Numerical modeling of wave interactions with coastal structures by a constrained interpolation profile/immersed boundary method, International Journal for Numerical Methods in Fluids, 2016b, 81(5): 265-283.

Zhao, X., Ye, Z. and Fu, Y.: Green water loading on a floating structure with degree of freedom effects, Journal of Marine Science and Technology, 2014, 19(3):302-313.